Evaluation of mean and intraseasonal variability of Indian summer monsoon simulation in ECHAM5: identification of possible source of bias

S. Abhik · P. Mukhopadhyay · B. N. Goswami

Abstract The performance of ECHAM5 atmospheric general circulation model (AGCM) is evaluated to simulate the seasonal mean and intraseasonal variability of Indian summer monsoon (ISM). The model is simulated at two different vertical resolutions, with 19 and 31 levels (L19 and L31, respectively), using observed monthly mean sea surface temperature and compared with the observation. The analyses examine the biases present in the internal dynamics of the model in simulating the mean monsoon and the evolution of the boreal summer intraseasonal oscillation (BSISO) and attempts to unveil the reason behind them. The model reasonably simulates the seasonal mean-state of the atmosphere during ISM. However, some notable discrepancies are found in the simulated summer mean moisture and rainfall distribution. Both the vertical resolutions, overestimate the seasonal mean precipitation over the oceanic regions, but underestimate the precipitation over the Indian landmass. The performance of the model improves with the increment of the vertical resolution. The AGCM reasonably simulates some salient features of BSISO, but fails to show the eastward propagation of the convection across the Maritime Continent in L19 simulation. The propagation across the Maritime Continent and tilted rainband structure improve as one moves from L19 to L31. The model unlikely shows prominent westward propagation that originates over the tropical western Pacific region. L31 also produces some of the observed characteristics of the northward propagating BSISOs. However, the northward propagating convection becomes stationary in phase 5–7. The simulation of shallow diabatic heating structure and the heavy rainfall activity over the Bay of Bengal indicate the abundance of the premature convection-generated precipitation events in the model. It is found that the moist physics is responsible for the poor simulation of the northward propagating convection anomalies.

Keywords Indian summer monsoon · Boreal summer intraseasonal oscillation · Vertical resolution · AGCM · Moist processes

1 Introduction

Indian summer monsoon (ISM) experiences intraseasonal oscillations (referred here as the boreal summer intraseasonal oscillations; BSISOs) in the form of enhanced (active) and reduced (break) spells of precipitation over the central and northern regions of Indian subcontinent (Ramamurthy 1969). The quasi-periodic variability of BSISO determines the strength of the seasonal mean monsoon (Goswami and Ajaya Mohan 2001; Goswami et al. 2006). The seasonal mean and the intraseasonal variability of the ISM rainfall have significant influence on the socio-economical growth of the Indian subcontinent. As a consequence, the prediction of active and break spells of ISM at least 2–3 weeks in advance has been received great attention over the decades (Goswami 2011; Suhas et al. 2012). The intraseasonal variability of the ISM represents much higher amplitude than the inter-annual variability of the seasonal mean (Waliser 2006; Goswami 2011). This inherent feature of the BSISO leads to achieve the potential predictability of 25–30 days. However, BSISO exhibits more complex nature than its boreal wintertime counterpart, eastward propagating Madden–Julian

S. Abhik · P. Mukhopadhyay (✉) · B. N. Goswami
Indian Institute of Tropical Meteorology, Dr. Homi Bhabha Road, Pashan, Pune 411008, India
e-mail: parthasarathi64@gmail.com; mpartha@tropmet.res.in

Oscillation (MJO, Madden and Julian 1971, 1972, 1994). During boreal summer (June to September, JJAS), the off-equatorial monsoonal heating modifies the eastward propagation; as a result BSISO shows both the eastward and northward propagation with a periodicity of 30–60 days (Wang 2011).

The ability to represent the complexity of the BSISO in the current general circulation models (GCMs) remains a great challenge (Waliser et al. 2003; Kim et al. 2008; Jiang et al. 2011). The GCMs mostly fail to capture the realistic seasonal cycle and the space–time characteristics of the intraseasonal variability of the ISM (Goswami 2011). Waliser et al. (2003) shows that the atmospheric general circulation models (AGCM) fail to represent the eastward propagating convection and the northwest-southeast-tilted rainband associated with the BSISOs. Analyzing 14 ocean–atmosphere coupled GCMs (CGCM) participating in the Fourth Assessment Report (AR4) of intergovernmental panel on climate change (IPCC), Lin et al. (2008) indicates that most of the models overestimate the near-equatorial precipitation and underestimate the variability of the northward propagating BSISO and westward propagating 12–24-day mode. Sperber and Annamalai (2008) show that the lack of the eastward propagating convection across the Maritime Continents is one of the major biases causing the unusual tilting of the rainband in CGCMs. Joseph et al. (2012) show that the mean ISM and its subseasonal variability are weakly simulated in SINTEX-F2 (atmosphere–ocean coupled ECHAM5) model. They identify that the weak meridional gradient of the seasonal mean easterly shear and tropospheric temperature (TT) gradient are primarily responsible for the weak monsoon circulation in the model. The model deficiencies are also attributed to the warmer sea surface temperature (SST) over the Indian Ocean (IO). The role of the atmosphere–ocean coupling and the explicit representation of the convection on the summer monsoon simulation are examined by Demott et al. (2011). Interestingly, the subseasonal tropical variability in the model is improved with the implementation of both the air-sea coupling and the super-parameterization. However, the improvement due to the air-sea coupling on the simulation of the tropical subseasonal variability is sensitive to the model (Kemball-Cook et al. 2002; Zhang et al. 2006). Other than the air-sea coupling, the convective parameterization (Slingo et al. 1996; Zhang and Mu 2005), background state (Slingo et al. 1996; Sperber et al. 2005) and the resolution of the model (Inness et al. 2001) may cause the uncertainty in the simulation of the tropical subseasonal variability.

Although substantial progress has been made in the simulation of the BSISO during the last two decades, the understanding of the northward propagating mechanisms remains incomplete. Several theoretical and observational studies highlight the mechanisms associated with the northward propagation of BSISO (Webster 1983; Wang and Xie 1997; Lawrence and Webster 2002 and Jiang et al. 2004). In recent times, Jiang et al. (2011) and Abhik et al. (2013, hereafter A13) identify the role of cloud processes on the northward propagation of BSISOs and A13 propose a mechanism based on the feedback between the convection and the atmospheric dynamics. The study demonstrates how the moisture condensation processes within the lower troposphere ahead of the convection and the sub-grid scale eddy heat transport in the boundary layer (PBL) induce the lower atmospheric instability essential for triggering the deep convection to the north of the existing convection. In addition, the strong updraft motion inside the deep convection allows the mixed and ice-phase hydrometeors to form in the middle and upper troposphere that helps to enhance the upper level divergence and lower level convergence through the release of the latent heat. The anvils of the deep convective clouds, mostly comprise of cloud ice, are likely to extend southward from their originating deep convection and remain aloft for the longer duration. Similar microphysical distributions of cloud liquid water (CLW) and cloud ice (CICE) are also reported by Jiang et al. (2011) using CloudSat data. These studies unveil a new framework to examine the BSISO in the backdrop of observed cloud processes. However, presence of such observed processes have not been explored in the current GCMs. Therefore, the fidelity of the GCMs in capturing the proposed mechanism for the northward propagation of BSISO is required to be examined. Moreover, the failure of coupled-ECHAM5 in simulating various aspects of BSISO in Joseph et al. (2012) also indicates further assessment of the internal dynamics of the ECHAM5 AGCM that significantly contributes to reproduce realistic BSISO signals.

Keeping these aspects in background, the present study attempts to diagnose the BSISO simulation in an AGCM at two different vertical resolutions. Inness et al. (2001) show that the increased vertical resolution improves the simulation of the midlevel convection associated with the tropical intraseasonal oscillations. Liess and Bengtsson (2004) argue that spatial structure of simulated intraseasonal variability is not sensitive to the vertical resolution. However, the discrepancy may arise from inappropriate ratio of vertical and horizontal resolution of the model. Roeckner et al. (2006) discuss the requirement of balance between horizontal and vertical resolution on global climate simulation. They indicate that the increased vertical resolution in ECHAM5 not only improves the performance of the model, but also enhances the computational efficiency. So, it is meaningful to examine the role of vertical resolution as the higher vertical resolution has the potential to simulate the vertical structure of the cloud correctly and

better representation of the vertical distribution of heating in the troposphere. In the present study, ECHAM5 (Roeckner et al. 2003) is chosen because it shows certain ability to reproduce some of the features of the BSISO (Liess et al. 2005, Sperber and Annamalai 2008, Joseph et al. 2012). Additionally, ECHAM5 is among the few AGCM which has a reasonable cloud microphysics to include the warm and cold cloud processes.

The description of the model, various observational dataset utilized for the evaluation of the simulations and the adopted methodologies are discussed in Sect. 2. Section 3 describes the ability of the model to simulate the mean-state of ISM, intraseasonal variability and northward propagation of BSISO. The major conclusions and findings of the study are summarized in the Sect. 4.

2 The model, observations and methodology

The spectral ECHAM5 (version 5.4, Roeckner et al. 2003) AGCM at a horizontal resolution of T106 is used in this study. Two identical experiments are performed with standard 19 vertical levels and the higher resolution with 31 levels (hereafter referred as L19 and L31, respectively) extending from surface to 10 hPa. The geometrical grid spacing in the free troposphere of L19 (L31) resolution increases gradually with height from about 1 km (500 m) in the lower troposphere, to 1.5 km (750 m) in the middle troposphere, and 2 km (1 km) around the tropopause (Roeckner et al. 2006). However, the top three and the bottom three levels are identical in both the resolutions. The mass flux scheme (Tiedtke 1989) with shallow, mid-level and deep convection (modified according to Nordeng 1994) is employed to parameterize the convection. The bulk cloud microphysics (Lohmann and Roeckner 1996) includes the prognostic equations for three phase (vapor, CLW and CICE) hydrometeors. In the experiments the AGCM is integrated for 12 years (1981–1992), but first year is discarded to avoid the influence of the model spin-up. The model is forced with observed monthly mean SST from the boundary conditions of atmospheric model intercomparison project II experiments. It should be noted that Fu and Wang (2004) and Seo et al. (2007) discuss the usefulness of monthly mean SSTs as the boundary forcing of AGCM over the use of daily or weekly mean SSTs.

The simulations are validated with various observed dataset over the JJAS period of 1998–2008. The Modern Era Retrospective-analysis for Research and Applications (MERRA, Bosilovich and coauthors 2006) daily averaged zonal wind (U), temperature, specific humidity dataset with 1.25° longitude × 1.25° latitude are utilized in this study. Daily Global precipitation Climatology Project (GPCP, Huffman et al. 2001) one-degree daily rainfall data for the

period of 1998–2008 is used to evaluate the precipitation from ECHAM5. Additionally, the simulated precipitation over the Indian land-points is also validated using gridded 1° × 1° daily rainfall dataset from India Meteorological Department (IMD, Rajeevan et al. 2006).

The daily anomalies of each meteorological field for both the observed dataset and model output are computed by subtracting the annual cycle (defined by the sum of annual mean and the first three harmonics) of each year. Further, a 20–90-day band-pass filter (Duchon 1979) is applied to extract the BSISO signal. An extended empirical orthogonal function (EEOF) analysis over the region 60°–95°E, 12°S–30°N is performed during May–October months of the 11 years. A temporal lag of 15 days with 1 day interval is applied to the filtered rainfall dataset for EEOF analysis. The first two principal components (PC1 and PC2) from EEOF analysis are considered to represent the spatio-temporal evolution of BSISO. Similarly, the 20–90-day band-pass filtered precipitation anomalies from the model are projected onto the observed EEOFs to obtain the corresponding PCs. It may be noted that Suhas et al. (2012) develop a real-time monitoring index for the identification of the BSISO over ISM region using similar technique. The present technique slightly differs from Suhas et al. (2012) such that we use 20–90-day filtered rainfall dataset over May to October months instead of longitudinally averaged unfiltered dataset over JJAS period. However, the analysis is not much sensitive to the deviation in the methodologies.

Furthermore, the diabatic heating (Q_1) is calculated following Yanai et al. (1973) as

$$Q_1 = C_p \left(\frac{p}{p_0}\right)^{R/C_p} \left(\frac{\partial \theta}{\partial t} + \vec{V}.\nabla \theta + \omega \frac{\partial \theta}{\partial p}\right) \qquad (1)$$

where C_p is the specific heat of air at constant pressure ($\sim$1,004 J kg^{-1} K^{-1}), R is the gas constant for dry air ($\sim$287 J kg^{-1} K^{-1}), p_0 is the reference pressure ($\sim$10^5 Pa) and θ is the potential temperature of the air parcel.

3 Results and discussions

3.1 Simulation of ISM mean-state by ECHAM5

We first examine the model performance in simulating the mean monsoon during boreal summer. Figure 1 shows the observed and simulated JJAS seasonal mean rainfall (mm day^{-1}) and 850-hPa wind (m s^{-1}) field over the ISM region. In GPCP (Fig. 1a), the precipitation maxima are observed over the Western Ghats and along the eastern shore of the Bay of Bengal (BoB). The observed (MERRA) mean 850-hPa wind maximum is located over the northern

IO over the latitude belt of 10°–15°N. The model, at both the vertical resolutions (Fig. 1b, 1c), underestimates the precipitation amount over the northern BoB, central and eastern Indian subcontinent and overestimates it mainly over the oceanic region. The rainfall bias over the equatorial Indian Ocean (EIO) appears to be improved with the increase of vertical level from 19 to 31. However, the higher vertical resolution (L31) is unable to reduce the wet bias over the BoB. The precipitation distribution (Fig. 1c) also appears to be zonally oriented in contrast to the observed north-west to south-east orientation of the intertropical convergence zone. The observed 850-hPa wind features are well captured at both the vertical resolutions.
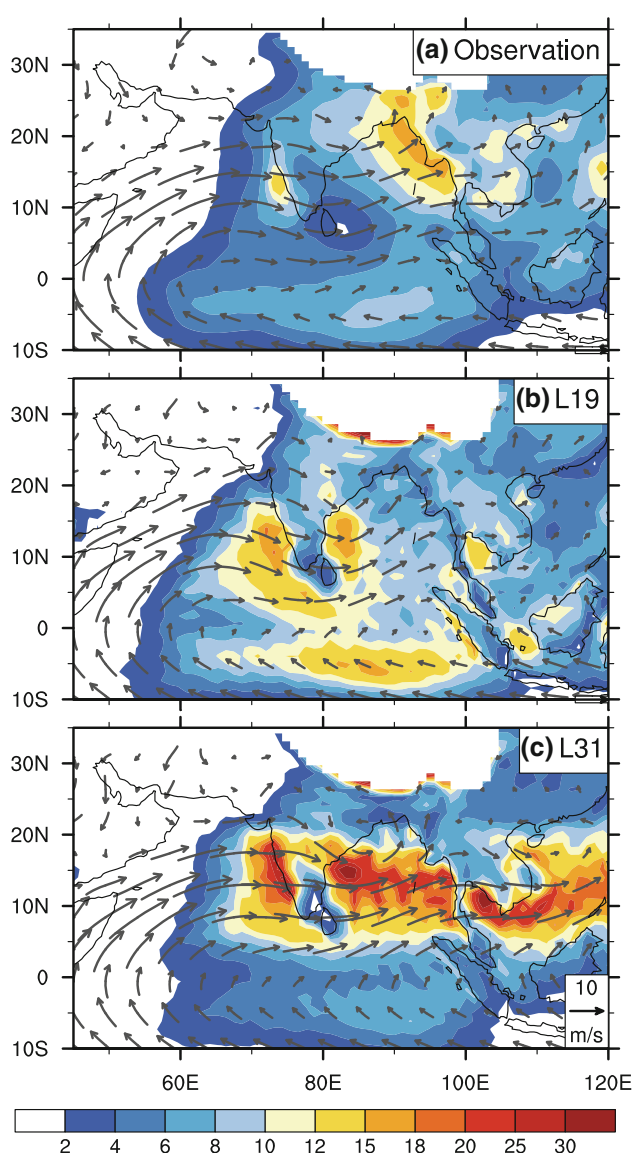
In L31, the westerlies over the northern IO are slightly stronger than the observation.

The biases in the other important dynamical and thermodynamical variables associated with the seasonal mean ISM (averaged between 65° and 95°E during JJAS), namely easterly wind shear (difference between zonal wind at 200 and 850 hPa), low-level specific humidity (averaged between surface and 850 hPa), tropospheric temperature (TT; averaged between 600 and 200 hPa) and equivalent potential temperature (θ_e; averaged between 1,000 and 850 hPa) are diagnosed in Fig. 2. Figure 2a shows the easterly wind shear from observation (MERRA reanalysis; red line) and the model (L19: green and L31: blue). Jiang et al. (2004) proposed that the mean easterly shear is one of the key parameter for the poleward propagation of the convection band. In L19, the strength of the easterly shear is significantly underestimated over the ISM region. L31 simulation shows an improvement in ability to produce the easterly shear in all the latitudes to the north of the Equator.

The moisture-convection feedback mechanism (Jiang et al. 2004) explains the northward propagation near the Equator. The interaction between seasonal mean low-level moisture and the mean flow contributes to the moisture-convergence to the north of the convection. However, the model seems to have serious bias in simulating the seasonal (JJAS) mean specific humidity field at the surface especially over the northern latitudes (Fig. 2b). It shows much weaker meridional gradient of mean surface specific humidity compared to observation. L19 (green) and L31 (blue) both underestimate the specific humidity over the region between the Equator and 25°N. The bias in the mean surface specific humidity is slightly improved in L31 simulation, but it still produces significantly weaker magnitude compared to the MERRA reanalysis.

The JJAS mean TT (Fig. 2c) and its north–south gradient is reasonably well simulated in ECHAM5. The simulation of TT gradient improves as the vertical resolution increases from L19 (green) to L31 (blue). It is noteworthy that the AGCM alone exhibits improvement over the simulation of easterly shear and TT gradient in the coupled ECHAM5 shown in Joseph et al. (2012). They identify that the weak TT gradient leads to the weakening of the easterly shear and the moisture gradient in the coupled model. We argue that a systematic connection between TT gradient and moisture distribution is unlikely. In ECHAM5, the improvement in the simulation of TT gradient is not reflected in the specific humidity pattern.

Weaker mean specific humidity may be responsible for the simulation of less instability in the PBL of the model (Fig. 2d). The seasonal mean lower atmospheric convective instability is represented in terms of θ_e averaged between surface and 850 hPa. At both the vertical resolutions, the magnitudes of the simulated θ_e are weaker than

Fig. 1 June–September (JJAS) mean rainfall (shaded, mm day^{-1}) and 850 hPa wind (vector, m s^{-1}) from **a** GPCP and MERRA reanalysis, **b** L19, **c** L31 simulation

Fig. 2 Seasonal mean meridional distribution of **a** easterly wind shear (U200–U850, m s^{-1}), **b** surface level specific humidity (g kg^{-1}), **c** tropospheric temperature (averaged between 200 and 600 hPa) and **d** equivalent potential temperature (averaged between 1,000 and 850 hPa) averaged between 65° and 95°E
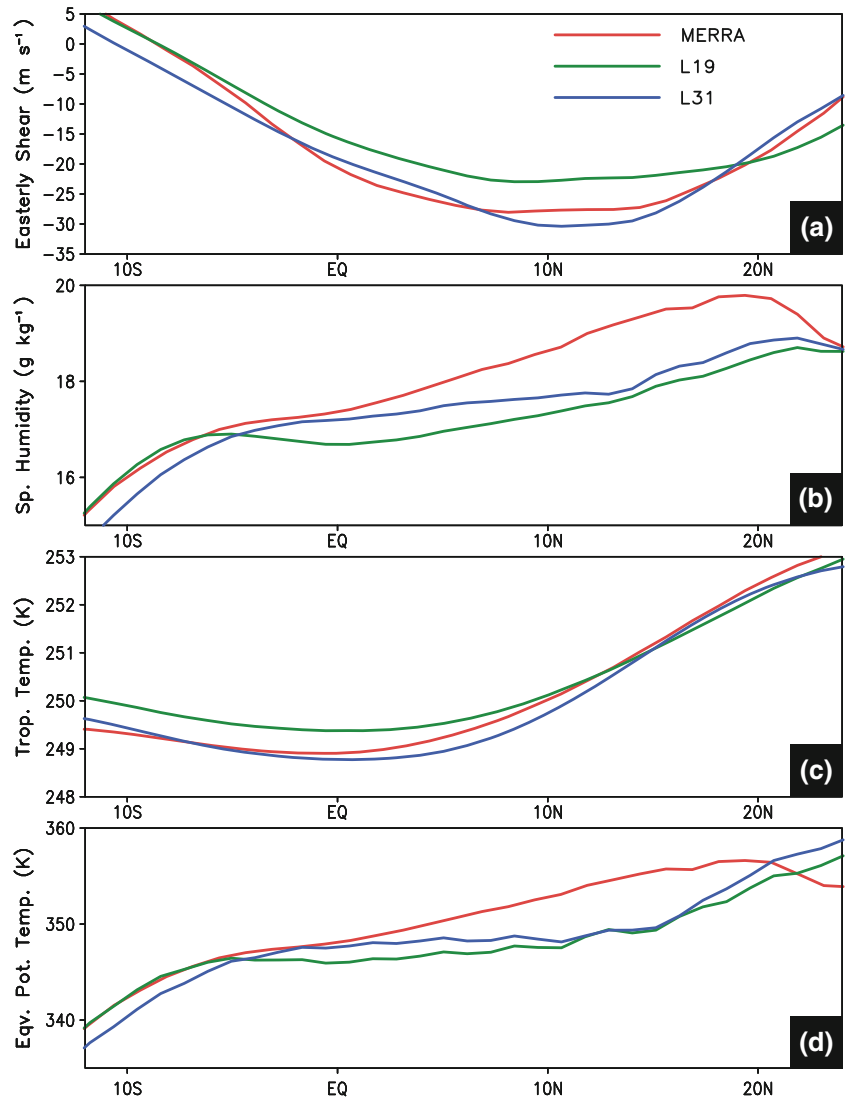

the observed over the northern tropical latitudes (Equator to 20°N). These fields will essentially influence the convection anomalies over this region and may finally influence the rainfall distribution in the model.

The fidelity of the model to simulate the seasonal mean ISM and its variability at two different vertical resolutions is summarized in the Taylor diagram (Taylor 2001) (Fig. 3). The JJAS mean spatial pattern correlation, root-mean square difference (RMSE) and the simulated to observed ratio of the variances of rainfall, wind, temperature and humidity over 40°–120°E, 15°S–30°N are assessed in Fig. 3. The distance from the origin indicates the normalized standard deviation of each variable, while the cosine of the angle swept out by the position vector from the origin indicates the pattern correlation between observed and simulated variable. The distance from the reference point (marked by solid red dot) to the plotted point denotes the RMSE. The isocircles (grey concentric

circles) of RMSE are drawn based on the skill score calculation using normalized standard deviation and the correlation coefficient. An accurately simulated variable that has least RMSE, highest correlation and normalized standard deviation close to the unity, should be placed close to the reference point. Figure 3 indicates that the model reasonably produces some of the metrics associated with the ISM e.g. TT, zonal wind at 850 hPa (U850), zonal wind at 200 hPa (U200). However, the L31 better reproduces the observed space–time structure of those variables with respect to its counterpart L19. But the performance of the model in the simulation of ISM precipitation and surface specific humidity at both the resolutions does not improve significantly. The precipitation and the lower level moisture biases indicate the requirement of further improvement to the cloud processes in the model.

Since precipitation is episodic as well as it exhibits variability in frequency, intensity and amount, a detailed
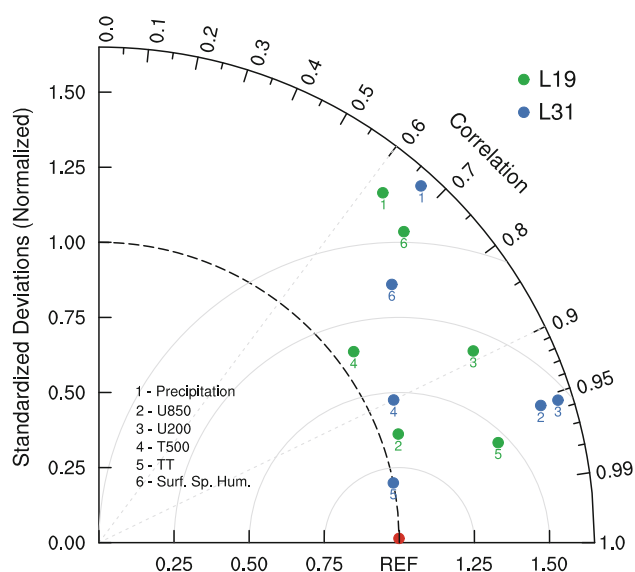
Fig. 3 Taylor diagram for ECHAM5 model at two vertical resolutions (L19 and L31) to summarize the relative skill to simulate the mean meteorological fields over the region 40°–120°E, 15°S–30°N during boreal summer season (JJAS). *Red dot* denotes the reference point

analysis of the precipitation characteristics are essential (Dai 2006). Hirons et al. (2012) use the probability distribution function (PDF) of rainfall to show how far the convective entrainment formulation is sensitive to the simulation of MJO in ECMWF model. They indicate that the PDF matches well with the observation when one moves from moisture convergence based formulation to the relative humidity dependent formulation. It is also shown that such modification increases the congestus cloud population in the mid-troposphere and decreases the shallow and deep convective clouds in the lower and upper troposphere. In the present study, we examine the PDF of daily rainfall (Fig. 4) during all JJAS periods for three rain-rate categories (lighter: <10 mm day^{-1}, moderate: 10–40 mm day^{-1} and heavy: >40 mm day^{-1} following Mukhopadhyay et al. 2010) over four different regions: Indian landmass only, core Indian monsoon zone (as defined in Rajeevan et al. 2010), BoB and EIO region (75°–95°E, 5°S–5°N). We believe that the biases in different rainfall categories will eventually contribute to the bias in the daily mean rainfall. Figure 4a shows the PDF of rainfall from GPCP (red curve), IMD (black curve), L19 (green curve) and L31 (blue curve) over the Indian land-mass only. The lighter rainfall is found to have higher contribution to the observed total rain from GPCP and IMD. L19 overestimates the lighter rainfall and underestimates the moderate rain-rate. This bias appears to be reduced with the increase of vertical resolution from L19 to L31; however, the lighter rain-rate is still overestimated. The problem seems to be more prominent over the core Indian

monsoon zone in L19 (Fig. 4b). But the bias in lighter rain-rate category is reduced in L31. It is also reported that the current GCMs have a tendency to overestimate the lighter rain (Dai 2006). The moderate and heavy rain-rate categories are significantly underestimated over the land-points in the model, particularly in L19 simulation (Fig. 4a, b). Over the BoB (Fig. 4c), the PDF shows a similar feature to that over the Indian land. In L31, however, the heavy (lighter) rainfall is overestimated (underestimated). The excessive contribution from the heavy rain-rate category may be responsible for the seasonal wet bias over the BoB in L31 (Fig. 1c). It is likely that the inefficiency of the convective parameterization may be responsible for the unrealistic precipitation distribution in the model. However, the rainfall distribution in L31 is reasonably improved over the EIO, where all three rain-rate categories are simulated with better degree of accuracy (Fig. 4d).

3.2 Monsoon intraseasonal variability

In the following analyses, the performance of the model in the simulation of BSISO is examined. The wavenumber-frequency analysis (Hayashi 1982, Teng and Wang 2003), in the meridional direction, is carried out to quantify the northward propagating variability over Indian sector (65°–95°E, 15°S–30°N). The spectra were calculated by Fourier transforming seasonal cycle removed GPCP precipitation data over 184 day segments from May to October each year and then averaging over all the years. Figure 5 shows the precipitation and MERRA 850 hPa zonal winds (U850) variance associated with the meridional propagating oscillations for observations and model. In the observation, northward propagating BSISO prefers the wavenumber one spatial scale with the 40–50 day temporal scale (Fig. 5a). A comparison between L19 and L31 indicates (Fig. 5b, c, respectively) that both the resolutions exhibit qualitatively similar spectral characteristics, although the latter simulates more realistic temporal scale. In L19, the peak appears at the lower frequency than in observation. L31 produces spectral peak similar to the observed mode. Consistent with Joseph et al. (2012), the spectral power is reduced by 40 % in the model.

To examine the eastward propagating equatorial low-frequency ISOs during boreal summer, wavenumber-frequency spectra of GPCP rainfall and U850 in the east–west direction between 10°S and 10°N are computed based on the Climate Variability and Predictability (CLIVAR) Research Program MJO Working Group (CLIVAR Madden-Julian-Oscillation Working Group 2009). In observations (Fig. 6a), the eastward propagation is dominant with periodicity of 30–60 days and a zonal scale between wavenumber 1 and 3. L19 fails to simulate significant spectral peaks at the eastward propagating BSISO spatial

Fig. 4 Probability distribution function (PDF) of daily rainfall (mm day^{-1}) during 11 JJAS seasons with a bin width of 5 mm day^{-1} in percentage over **a** Indian landmass, **b** monsoon zone (as defined by Rajeevan et al. 2010), **c** Bay of Bengal and **d** equatorial Indian Ocean (75°–95°E, 5°S–5°N)
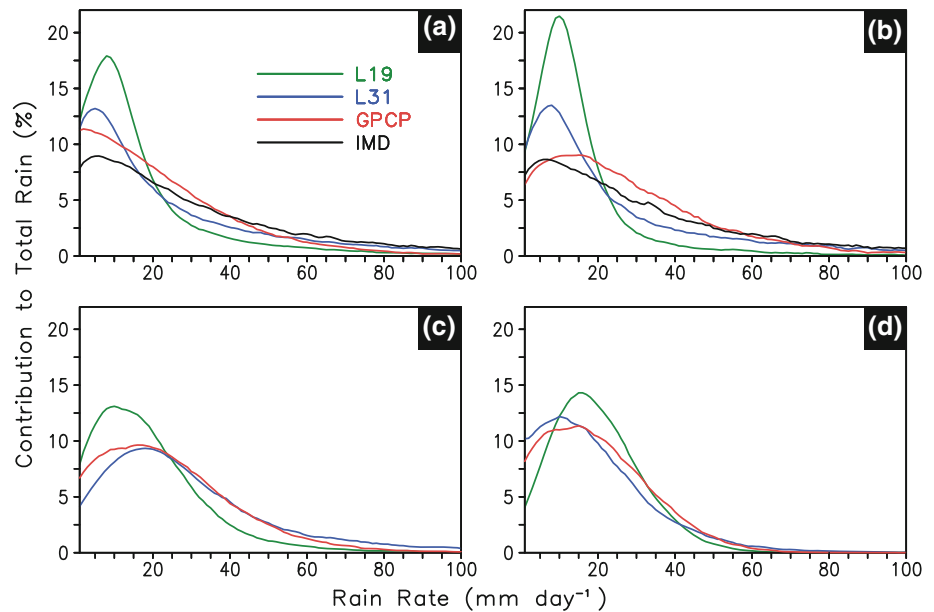

and temporal scales (Fig. 6b). The eastward propagation is concentrated at lower frequencies (period >60 day) and the wavenumber with maximum power is shifted to higher wavenumber side. Interestingly, the spectral characteristics improve with the higher vertical resolution (Fig. 6c). For U850, L31 resolution produces a spectrum similar to the observation, although the power is underestimated. In contrast, the model is unable to produce the spectral peak for the precipitation. The maximum power is distributed over the wavenumber range 1–3 with different periodicities. This indicates a lack of coherence between the intraseasonal zonal wind and precipitation simulation in the model.

The 20–90 day filtered JJAS intraseasonal variance of precipitation and U850 in observation and the model are shown in Fig. 7. The intraseasonal variance of observed rainfall shows the maxima at three different locations over south Asia: Western Ghats, BoB and western Pacific warm pool region (Fig. 7a). Additionally, another secondary maximum is also notable over the eastern equatorial Indian Ocean (EEIO) associated with the eastward propagation of BSISO. Both the zonal wind and precipitation variance over the tropics are concentrated in the summer hemisphere. In L19, the precipitation variability over the BoB is limited along the eastern coastline of India and it is very weak over the western Pacific Ocean (Fig. 7b). However, the EEIO rainfall variability is overestimated in L19 and the corresponding maxima is slightly shifted to the west. L31 overestimates the precipitation variability over the entire south Asia and western Pacific Ocean (Fig. 7c). However, model simulates improved precipitation variability over the EEIO region due to increased vertical resolution.
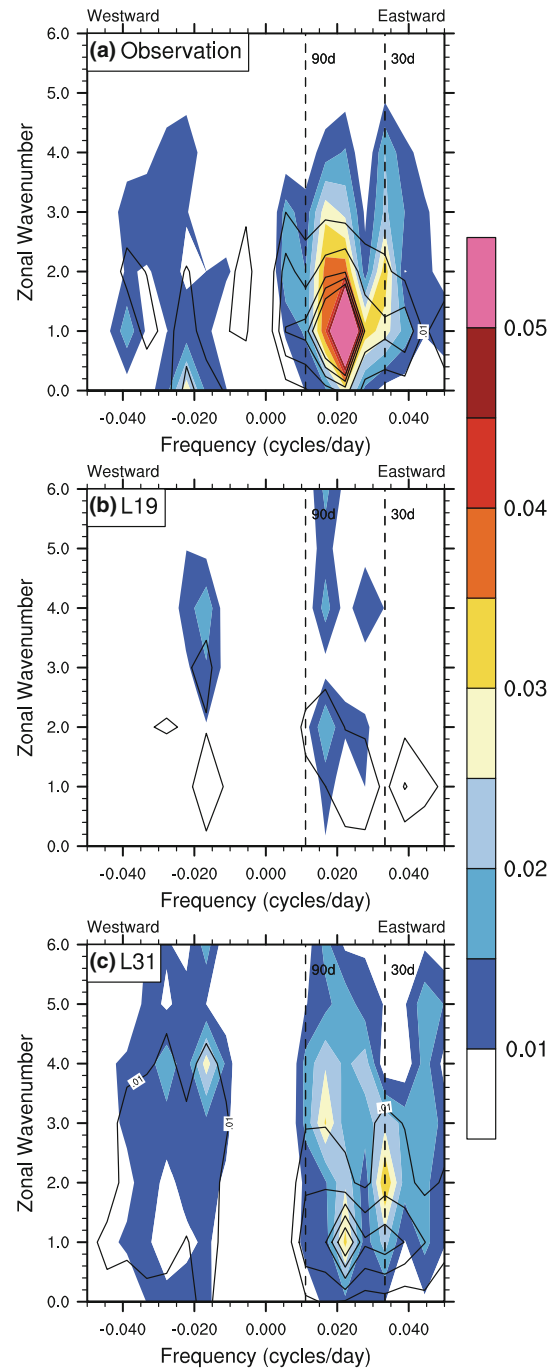
Figure 8 shows the time lag-correlation analysis of 20–90 day filtered precipitation (colors) and U850 (lines) averaged between 10°S and 10°N correlated with a time series of intraseasonal filtered precipitation averaged over the EEIO region (10°S–5°N, 75°–100°E) for boreal summer. The time lag-longitude correlation analysis over that region (Fig. 8a–c) provides the spatiotemporal characteristics of the eastward propagating BSISO. The observed BSISO first appears in the western Indian Ocean that further propagates into the western Pacific Ocean and finally decays near the date line (Fig. 8a). It shows the eastward phase speed across the region of about 3.5° per day. Easterly (westerly) zonal wind at 850 hPa leads (lags) the precipitation anomaly by about 5–7 days and the zonal wind anomaly shows faster eastward propagation after the decay of precipitation anomaly. L19 simulates the eastward propagation with faster phase speed and that fails to propagate beyond 100°E, across the Maritime Continent (Fig. 8b). In contrast, L31 (Fig. 8c) simulates the eastward propagation with realistic phase speed but the correlation decays rapidly across the Maritime Continent. However, both the vertical resolutions of the model produce prominent westward propagation that originates over the tropical western Pacific region. The dominance of the westward propagating convective anomalies over the equatorial region inhibits the eastward propagation beyond Maritime continent in the model.

Similar time lag-correlation analysis is also performed using 20–90 day filtered precipitation time series over the BoB region (10°–20°N, 80°–100°E) and the same precipitation and U850 data averaged between 15° and 20°N (Fig. 9). In observation (Fig. 9a), the eastward propagating positive precipitation anomalies first develop around 50°E
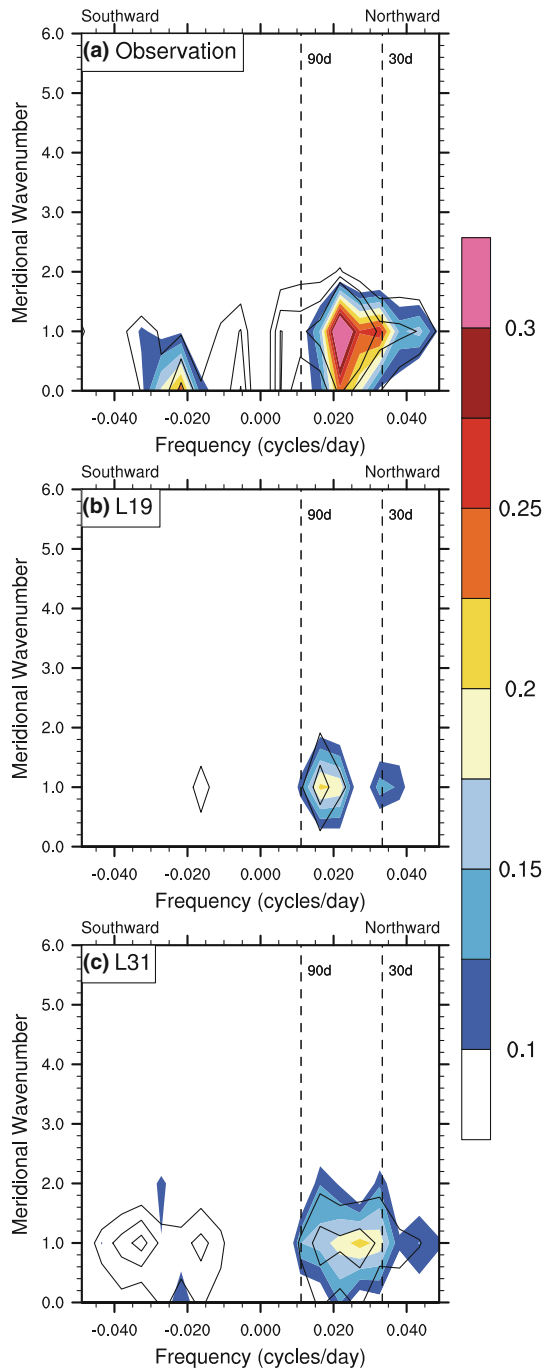
Fig. 5 Meridional wavenumber-frequency spectra during boreal summer over 15°S–30°N using precipitation (mm² day⁻², colors) and U850 (m² s⁻², lines) data averaged between 60° and 95°E for **a** GPCP and MERRA reanalysis, **b** L19, **c** L31 simulation

Fig. 6 Zonal wavenumber-frequency spectra during boreal summer using precipitation (mm² day⁻², color) and U850 (m² s⁻², line) data averaged between 10°S and 10°N for **a** GPCP and MERRA reanalysis, **b** L19 and **c** L31 simulation

at lag −15 and appear to amplify between 70° and 95°E from about lag −8 to 10. The 850-hPa zonal wind also exhibits characteristics qualitatively similar to Fig. 8a. However, both the vertical resolutions of the model poorly represent the observed features over 15°–20°N. L19 exhibits the dominance of westward propagation from the

central Pacific to the Indian region. Surprisingly, the periodicity of the westward propagating mode is almost similar to that of the observed eastward propagation (Fig. 9b). In contrast, the westward propagation in L31 resolution is limited in the 60°–120°E region (Fig. 9c) and the propagation is faster and of shorter duration than that of L19
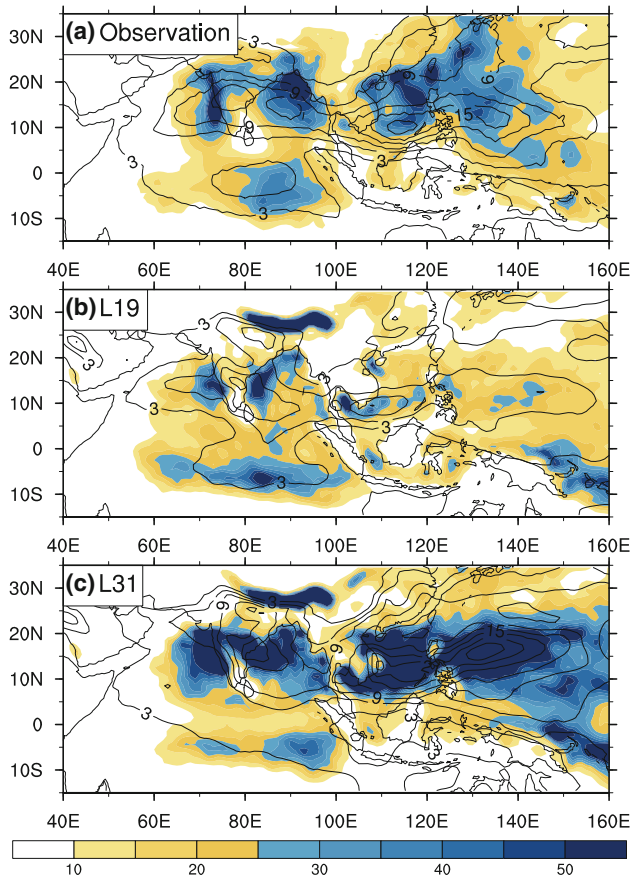
Fig. 7 Boreal summer (JJAS) 20–90 day filtered precipitation (mm^2 day^{-2}, color) and U850 (m^2 s^{-2}, line) variance for **a** GPCP and MERRA reanalysis, **b** L19, **c** L31 simulation

simulation. The quadrature relationship between precipitation and U850, unlike the observation, is also poorly simulated in the model.

3.3 Northward propagation in ECHAM5

In order to examine the spatio-temporal characteristics associated with the northward propagating BSISOs, composite BSISO events are computed. The BSISO events at different phases are composited on the basis of the BSISO indices (PC1 and PC2, defined as MISO1 and MISO2 respectively in Suhas et al. 2012) that constructed from EEOF analysis over the region 65°–95°E, 12°S–30°N (details in Sect. 2). Fig. 10 shows the life cycle of the 20–90 day filtered precipitation anomalies associated with the different phases of the northward propagating BSISO convection. In observation, Fig. 10a, the convective signal appears first over the EIO region in phase 1. Subsequently the convection intensifies and propagates eastward along the Equator in phases 2–3. In phase 3, it asymmetrically bifurcates with stronger anomalies in the northern hemisphere than its southern hemispheric component. Further
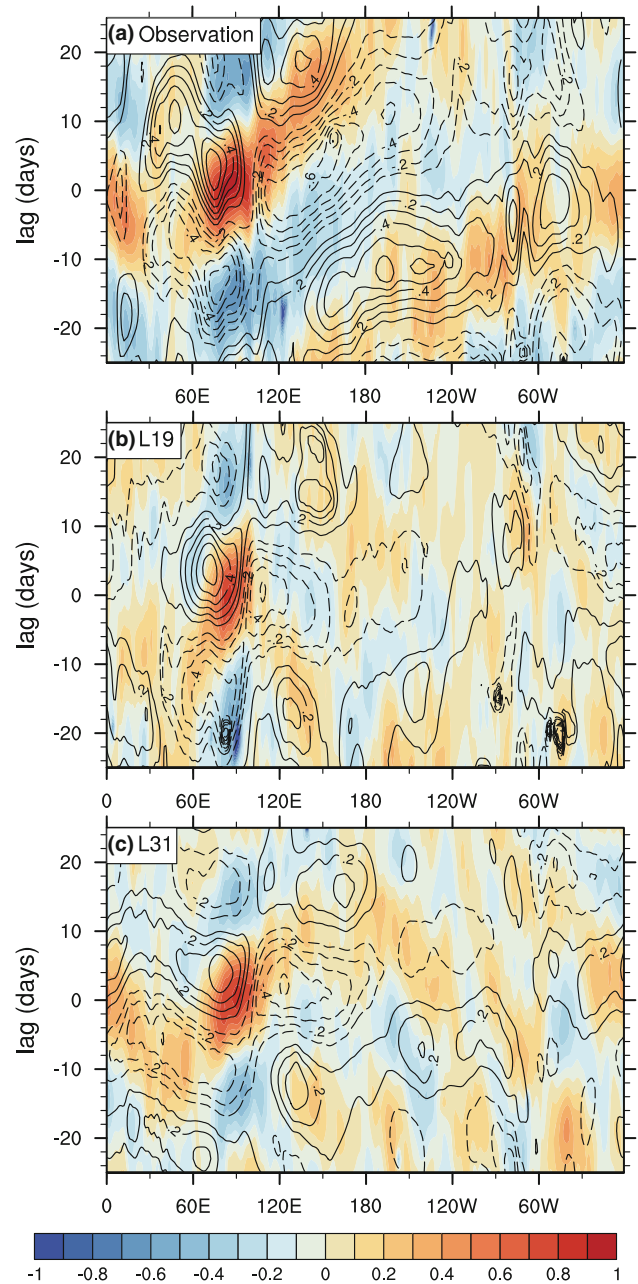
Fig. 8 Longitude versus lag correlation of 20–90-day filtered Indian Ocean precipitation (10°S–5°N, 75°–100°E) with 20–90-day filtered precipitation (*shaded*) and 850-hPa zonal wind (*contour*). Data are averaged between 10°S and 10°N for **a** GPCP and MERRA reanalysis, **b** L19, **c** L31 simulation

the convection propagates eastward across the Maritime Continent and towards north onto the Indian subcontinent, resulting northwest-southeast tilted rainband (phase 3–7). The role of Maritime Continent on the propagation of BSISO is reported by Zhu et al. (2010). In phase 8, the convection progresses further northward to the foothills of the Himalaya followed by the negative rainfall anomalies over the monsoon trough region. The dipole structure of